Journal of Applied Physics

First principles calculations of intrinsic mobilities in tin-based oxide semiconductors SnO, SnO_2, and Ta_2SnO_6

Cite as: J. Appl. Phys. **126**, 185701 (2019); https://doi.org/10.1063/1.5109265
Submitted: 09 May 2019 . Accepted: 09 September 2019 . Published Online: 08 November 2019

Yaoqiao Hu, Jeongwoon Hwang, Yeonghun Lee, Patrick Conlin, Darrell G. Schlom, Suman Datta, and Kyeongjae Cho

Journal of Applied Physics ARTICLE scitation.org/journal/jap

First principles calculations of intrinsic mobilities in tin-based oxide semiconductors SnO, SnO_2, and Ta_2SnO_6

Cite as: J. Appl. Phys. **126**, 185701 (2019); doi: 10.1063/1.5109265
Submitted: 9 May 2019 · Accepted: 9 September 2019 ·
Published Online: 8 November 2019

Yaoqiao Hu,[1] Jeongwoon Hwang,[1,2] Yeonghun Lee,[1] Patrick Conlin,[1] Darrell G. Schlom,[3,4] Suman Datta,[5] and Kyeongjae Cho[1,a)]

AFFILIATIONS

[1]Department of Materials Science and Engineering, The University of Texas at Dallas, Richardson, Texas 75080, USA
[2]Department of Physics Education, Chonnam National University, Gwangju, 61186 Republic of Korea
[3]Department of Materials Science and Engineering, Cornell University, Ithaca, New York 14853-1501, USA
[4]Kavli Institute at Cornell for Nanoscale Science, Ithaca, New York 14853, USA
[5]Department of Electrical Engineering, University of Notre Dame, Notre Dame, Indiana 46556, USA

[a)]**Author to whom correspondence should be addressed:** kjcho@utdallas.edu

ABSTRACT

The development of high-performance *p*-type oxides with high hole mobility and a wide bandgap is critical for the applications of metal oxide semiconductors in vertically integrated CMOS devices [Salahuddin *et al.*, Nat. Electron. **1**, 442 (2018)]. Sn^{2+}-based oxides such as SnO and $K_2Sn_2O_3$ have recently been proposed as high-mobility *p*-type oxides due to their relatively low effective hole masses, which result from delocalized Sn s-orbital character at the valence band edge. Here, we introduce a promising ternary Sn-O-X compound, Ta_2SnO_6, which exhibits strong valence band dispersion and a large bandgap. In order to evaluate the performance of this oxide as a p-type semiconductor, we perform first-principles calculations of the phonon-limited room-temperature carrier mobilities in SnO, SnO_2, and Ta_2SnO_6. Electron relaxation time is evaluated, accounting for the scatterings from acoustic deformation potentials and polar optical phonons (POP), within the isotropic and dispersionless approximation. At room temperature, the electron/hole mobilities in a given material (SnO, SnO_2, and Ta_2SnO_6) are found to be limited by POP scattering. SnO_2 shows high room-temperature electron mobility of 192 $cm^2/(V\,s)$, while SnO and Ta_2SnO_6 exhibit impressive hole mobilities, with the upper limit at 60 and 33 $cm^2/(V\,s)$, respectively. We find that carrier effective mass largely accounts for the differences in mobility between these oxides with correspondingly different POP scattering rates. The theoretically predicted intrinsic mobilities of each material will provide the upper limit to the real mobilities for their device applications. Our findings also suggest a necessity of further investigation to identify even higher mobility p-type oxides with smaller hole effective masses.

I. INTRODUCTION

Monolithic 3D integration or vertical CMOS is considered an attractive option for hyperscaling integrated circuits.[1,2] In vertical CMOS, multiple layers of logic circuitry and memory are vertically stacked so as to continue the exponential increase in the density of devices and alleviate the processing-storage communication bottleneck.[1–5] Vertical CMOS technology requires the upper layer circuits to be processed with a controlled thermal budget so as to not compromise the electrical quality of the lower front-end layers.[4,5] In addition, access transistors and peripheral logic transistors in the vertically stacked memory cells should exhibit high on-state drive current and low off-state current leakage.[1] Accordingly, the channel materials for the upper layer transistors should have a back-end-of-line (BEOL)-compatible low processing temperature (below 400 °C), a relatively large bandgap (>1.5 eV) to ensure ultralow current leakage, and good carrier mobility [>150 $cm^2/(V\,s)$ for electrons, >100 $cm^2/(V\,s)$ for holes] for high drive current.[1] Semiconducting metal oxides (MO) are promising candidates for vertical CMOS channel materials due to their ease of synthesis at low temperature and wide bandgap.[1,6,7] To date, these

metal oxide semiconductors have been almost exclusively studied as the transparent conducting electrodes for flexible electronics and optoelectronics.[8–11] For instance, indium tin oxide (ITO) films, with a bandgap ~3.75 eV, a resistivity as low as $10^{-4}\,\Omega$ cm, and electron mobility up to 100 $cm^2/(V\,s)$,[10] are widely used for transparent electrodes in flat-panel displays and thin-film solar cells.[8–13] For BEOL-compatible vertical FETs, high-mobility MO with bandgaps exceeding 1.5 eV appear attractive for n-channel transistors in the upper layers for applications as logic and memory access transistors.[1] However, most developed and commercialized oxide semiconductors are limited to *n*-type conduction, and *p*-type oxides have inferior performance due to carrier mobilities that are significantly lower than that of their *n*-type counterparts.[14] Developing high-mobility *p*-type oxides would enable a complementary transistor solution that provides more flexibility for the design and implementation of more efficient BEOL vertical CMOS devices.

The low hole mobilities in *p*-type oxides originate from the flat valence bands and the corresponding large effective mass of holes arising from the localized oxygen 2*p* orbitals at the valence band edge.[15,16] Introducing extended orbital electronic states at the valence band maximum (VBM) above the oxygen 2*p*-orbital would enable the development of high-mobility *p*-type oxides.[1] Such extended hybrid electronic states can be derived from a metal atom's *s* orbitals and would result in a very small hole effective mass. This effect can provide high hole mobilities since the underlying mechanism for high mobility of *n*-type oxides arises from the same *s* orbitals as empty states. Tin-based oxides such as SnO and $K_2Sn_2O_3$ have recently been shown to satisfy this condition, with the 5*s* orbital of Sn^{2+} forming the VBM.[16] The electronic band structures of SnO and $K_2Sn_2O_3$ have been calculated confirming the large band dispersion at the VBM, which corresponds to small hole effective mass values.[1,16] However, the bandgap of SnO (~0.6 eV) is too small for practical *p*-type oxide devices, and the marginal phase stability of $K_2Sn_2O_3$[16] can be a serious issue leading to K contamination of the surrounding device structures by phase changes of $K_2Sn_2O_3 \rightarrow KSn_2O_3 + K \rightarrow Sn_2O_3 + 2K$. Furthermore, a design rule based simply on the carrier effective masses does not provide quantitative mobility values, which incorporate carrier scattering rates. Although the small effective mass is a key characteristic useful for rapid screening of high hole mobility oxides, a detailed mobility calculation is critical to obtain more accurate values of the intrinsic mobilities and to confirm whether a candidate *p*-type oxide exhibits high hole mobility.

Recent electrical characterizations of *p*-type SnO have shown room-temperature carrier mobility in the range of 0.1–20 $cm^2/(V\,s)$,[6,17,18] values that are uncharacteristically low for a high-mobility *p*-type oxide. It is not well understood if the poor hole mobility can be improved for higher quality SnO samples. A crystalline phase-based mobility simulation does not necessarily represent the behavior of a practical device due to the polycrystal or amorphous nature of p-type oxides where more significant scattering mechanisms such as grain boundary scattering and surface scattering[19,20] are present. Despite this, the phonon-limited intrinsic mobilities provide an upper limit to the real values and help guide the material selection process. In order to design a p-type oxide with high mobility and stability, we started by varying the composition of $K_2Sn_2O_3$ to search for complex Sn-O-X ternary oxides with higher phase stability. Through this search process, we identified a promising candidate, Ta_2SnO_6, which is stoichiometrically equivalent to $Ta_2O_5 + SnO$. Compared to $K_2Sn_2O_3 = K_2O + 2SnO$, Ta_2O_5 is thermodynamically more stable than K_2O and also compatible with conventional device processing. Ta_2SnO_6 also exhibits a larger bandgap (>2 eV) than SnO as well as strong valence band dispersion, which are all promising characteristics. It is noted that another Sn^{2+}-based Sn-O-Ta ternary oxide $Ta_2Sn_2O_7$ has recently been investigated as a *p*-type oxide for its VBM containing Sn-5*s* orbital contribution.[21] However, $Ta_2Sn_2O_7$ is not promising because density functional theory (DFT) calculations show that its valence band edge is very flat and that $Sn_2Ta_2O_7$ is not thermodynamically most stable in the Sn-O-Ta ternary phase space.[22]

In this work, we report the calculations of both electron and hole mobilities in tin-based oxides including *p*-type SnO and Ta_2SnO_6 and *n*-type SnO_2. We study the phonon-limited intrinsic mobility values in these oxides, given that phonon scattering is the intrinsic scattering mechanism and often dominates at room temperature.[23] We formulate the scattering rate in the presence of multiple phonon modes, which we then use to determine carrier mobility. Our calculations show that SnO_2 is a good *n*-type semiconductor with high electron mobility, whereas *p*-type SnO and Ta_2SnO_6 exhibit slightly lower hole mobilities. The theoretically predicted intrinsic mobilities for SnO, Ta_2SnO_6, and SnO_2 provide the upper limit to the real mobilities for their device applications. Our results indicate a necessity of further investigation to identify *p*-type oxides with even higher mobility.

II. COMPUTATIONAL METHODOLOGY

The density functional theory (DFT) calculations were performed by using Vienna *ab initio* Simulation Package (VASP)[24,25] using projected augmented wave (PAW)[26,27] pseudopotentials. The Perdew-Burke-Ernzerhof generalized gradient approximation (GGA-PBE) functional was employed to depict the exchange-correlation potential energy. For all calculations, an energy cutoff of 520 eV was adopted for plane wave basis expansion. Brillouin zone integrations were performed based on the Gamma-centered Monkhorst-Pack k-point mesh, with sampling density varying with lattice constants to ensure the desired accuracy. Structures were relaxed using the conjugate gradient (CG) method with the convergence criterion of the force on each atom less than 0.02 eV/Å. The converged energy criterion is 10^{-5} eV for electronic minimization. The phonon frequencies at the Gamma point were calculated by using density functional perturbation theory (DFPT) as implemented in VASP. For electron-phonon coupling matrix elements evaluation, the phonopy code[28] was used to extract the force constant matrix from Hellmann–Feynman forces and to subsequently calculate the eigenfrequencies and eigendisplacements. Since the carrier mobilities are sensitive to the electronic structures, especially effective masses, we used the Heyd-Scuseria-Ernzerhof (HSE)[29] hybrid functional to obtain an accurate evaluation of effective masses and bandgaps. The screening parameter in HSE was fixed at 0.2 $Å^{-1}$ (HSE06), while the fraction of Hartree-Fock exchange (α) was varied in order to reproduce the known lattice constants and bandgaps. This fraction was finally tuned at $\alpha = 0.32$ for SnO_2 and $\alpha = 0.25$ for SnO, which yields consistent lattice constants and bandgaps when compared with

TABLE I. The HSE mixing parameter α, calculated lattice constants, and bandgaps in SnO, SnO_2, and Ta_2SnO_6. Experimental data are shown in parentheses.

	Crystal	α	a (Å)	b (Å)	c (Å)	E_g (eV)
SnO	Tetragonal	0.25	3.79 (3.80)[31]	3.79 (3.80)	4.95 (4.84)	0.6
SnO_2	Tetragonal	0.32	4.74 (4.74)[32]	4.74 (4.74)	3.18 (3.19)	3.6 (3.6–3.7)[33]
Ta_2SnO_6	Monoclinic	0.25	8.97	8.97	5.53	3.0

experiments (Table I). The bandgap of SnO predicted in this work stands somewhat lower than that in the reference work (0.84 eV)[30] because the bandgap of SnO is sensitive to the interlayer distance between SnO layers and the optimized c-axis lattice constant (4.95 Å, agreeing well with the experimental value 4.84 Å) is slightly smaller compared to the reference (5.03 Å).[30]

III. RESULTS AND DISCUSSION

A. Mobility theory

In the Boltzmann transport theory, the drift mobility is connected to conductivity through $\mu = \sigma/(ne)$, where σ is the conductivity, n is the carrier density, and e is the electron charge. Within the relaxation time approximation (RTA), the mobility is given by the well-known Drude expression,

$$\mu = \frac{e\langle\langle \tau_{\mathbf{k}} \rangle\rangle}{m^*}, \tag{1}$$

where $\tau_{\mathbf{k}}$ is the energy-dependent relaxation time and $\langle\langle\cdot\rangle\rangle$ indicates the energy-weighted average relaxation time and is defined as

$$\langle\langle \tau_{\mathbf{k}} \rangle\rangle = \frac{\int dE_{\mathbf{k}} D(E_{\mathbf{k}}) f(E_{\mathbf{k}}) \tau(E_{\mathbf{k}}) E_{\mathbf{k}}}{\int dE_{\mathbf{k}} D(E_{\mathbf{k}}) f(E_{\mathbf{k}}) E_{\mathbf{k}}}, \tag{2}$$

where E is the carrier energy, $D(E)$ is the density of states (DOS), $f(E) = 1/\{\exp[(E - E_F)/kT] + 1\}$ is the equilibrium distribution given by the Fermi-Dirac function, and E_F is the Fermi level. When the system is nondegenerate, the Fermi-Dirac distribution is usually approximated by the Boltzmann distribution. We will see that only electrons at the conduction band minimum (CBM) and holes at the VBM are relevant to the averaged relaxation time. In relatively pure crystalline samples with negligible impurities, the dominant scattering mechanism is electron-phonon scattering. In this case, the relaxation time, or scattering rate, is determined through Fermi's golden rule,[34]

$$\frac{1}{\tau_{\mathbf{k}}} = \frac{2\pi}{\hbar} \sum_{\lambda} \int_{BZ} d\mathbf{q} |g_{\mathbf{q}}^{\lambda}|^2 \delta(E_{\mathbf{q}+\mathbf{k}} - E_{\mathbf{q}} \mp \hbar\omega) \begin{Bmatrix} N_{\mathbf{q}} \\ N_{\mathbf{q}} + 1 \end{Bmatrix}. \tag{3}$$

Here, $\hbar$ is the reduced Planck constant, λ labels the phonon mode, $g_{\mathbf{q}}^{\lambda}$ is the matrix element for electron-phonon coupling, $N_{\mathbf{q}}$ is the phonon occupation number that is given by the Bose-Einstein distribution function, and upper and lower symbols represent absorption and emission, respectively. The Fermi-Dirac distribution for electrons does not appear in Eq. (3) since the carrier scattering rates will not depend on the electron distribution function when the low-field transport and isotropic scattering are considered.[35] Note that in this evaluation model, only the intraband scattering has been taken into account, since in the nondegenerate case and low-field transport condition, the phonon-induced potentials are not sufficiently strong to trigger the interband process. Finally, if more than one scattering mechanism exist, the total mobility, μ_{tot}, is given by Matthiessen's rule,

$$\frac{1}{\mu_{tot}} = \frac{1}{\mu_I} + \frac{1}{\mu_{II}} + \cdots, \tag{4}$$

where μ_I and μ_{II} represent the mobilities by the individual scattering mechanism.

B. Acoustic deformation potential (ADP) scattering

The acoustic deformation potential (ADP) scattering comes from the local changes of the crystal potential associated with a lattice vibration due to an acoustic phonon. This scattering is dominant in nonpolar semiconductors such as Si and graphene. In the presence of elastic scattering approximation, the relaxation time associated with the ADP scattering is given by[35]

$$\frac{1}{\tau_{\mathbf{k}}} = \frac{\pi D_A^2 k_B T}{\hbar \bar{C}_l} D(E_{\mathbf{k}}), \tag{5}$$

where T is the absolute temperature, $\bar{C}_l = (C_{11} + C_{22} + C_{33})/3$ is the average longitudinal elastic constant, and D_A is the acoustic deformation potential constant.[36] In the present work, the elastic constant is evaluated through the use of stress-strain relationships,[37] $C_{ii} = \frac{1}{V}\frac{\partial^2 E}{\partial \varepsilon_i^2}\Big|_0$, where V is the cell volume at equilibrium, E is the total energy, and ε_i is the strain along the ith axis. By quadratically fitting the total energy with respect to strain, one can obtain the elastic constant. The deformation potential constant is defined as[36] $\delta E = D_A \frac{\delta a}{a}$, where δE is the CBM or VBM change due to the uniaxial lattice deformation $\delta a/a$, where a is the lattice constant. Based on this definition, the deformation potential constant D_A can be calculated as[35] $D_A = \frac{\partial E}{\partial \varepsilon_V}\Big|_0$, where ε_V is the volumetric strain. By linearly fitting the total energy with respect to volume strain, one can obtain the deformation potential constant. In the case of parabolic band approximation, the 3D density of states (DOS) can be written as

$$D(E) = \frac{1}{2\pi^2} \left(\frac{2m_{dos}^*}{\hbar^2} \right)^{\frac{3}{2}} E^{\frac{1}{2}}, \tag{6}$$

where $m_{dos}^* = (m_x^* m_y^* m_z^*)^{1/3}$ is the density of states' effective mass. Combining Eqs. (2), (5), and (6), one obtains the ADP-limited

TABLE II. The elastic constants C_l, acoustic deformation potential constants D_A, carrier effective masses m^*, and ADP-limited mobilities μ_{ADP} in SnO, SnO_2, and Ta_2SnO_6. Values form other calculation works are shown in parentheses.

		C_l (GPa)					m^* (m_0)				μ_{ADP} (cm^2/V s)		
System		x	y	z	ave	D_A (eV)	x	y	z	dos	x	y	z
SnO	e	96	96	36	76	3.51	0.25	0.25	0.43	0.30	9308	9308	5411
	h					4.33	2.98 (2.80)[39]	2.98 (2.80)	0.64 (0.59)	1.78	35	35	164
SnO_2	e	210 (261)[40]	210 (261)	377 (472)	266	8.17	0.26 (0.26)[41]	0.26 (0.26)	0.21 (0.20)	0.24	7954	7954	9848
	h					2.06	1.27	1.27	1.60	1.37	1899	1899	1508
Ta_2SnO_6	e	187	192	199	193	1.35	2.20	31.6	0.83	3.86	392	27	1040
	h					2.80	8.4	0.72	0.98	1.81	74	868	638

mobility,[38]

$$\mu_\alpha = \frac{2\sqrt{2\pi}e\bar{C}_l\hbar^4}{3(k_BT)^{3/2}D_A^2 m_{dos}^{*\,3/2} m_{cond,\alpha}^*}, \tag{7}$$

where m_{cond}^* is the conductivity effective mass and is equal to the band effective mass and α is the Cartesian direction.

The computed elastic constant, deformation potential constants, and ADP mobility for SnO, SnO_2, and Ta_2SnO_6 are listed in Table II. Our calculated elastic constants for SnO_2 and hole effective masses for SnO are close to other calculation works.[39–41] For both p-type SnO and n-type SnO_2, the electron effective masses are lower than the hole effective masses. The asymmetry of effective masses between electrons and holes in SnO and SnO_2 accounts for the large difference of mobilities between the two types of carriers, as can be seen in Table II. At a low temperature ($T < 100$ K) where optical phonon scattering is suppressed, ADP scattering becomes a dominant factor in determining the intrinsic mobility. However, since there are no reports on low-temperature mobilities for SnO or SnO_2, we cannot validate our calculation results by comparing with experimental data. When compared with other nonpolar semiconductors such as Si where the intrinsic mobility is limited by ADP, SnO_2 shows both good electron mobility and hole mobility, while SnO exhibits a much lower hole mobility, though it even has higher electron mobility. Ta_2SnO_6 shows both satisfying electron mobility and hole mobility but with strong anisotropy along different directions due to the highly anisotropic effective mass values. Nevertheless, compared with ADP, POP scattering is more important in determining the room-temperature mobility for polar crystals and will be discussed in the next part.

C. Polar optical phonon scattering

Polar crystals contain two or more atoms in a unit cell with nonzero Born effective charge tensors. Lattice vibrations associated with polar optical phonons (POP) at a long wavelength give rise to macroscopic electric fields that can strongly scatter electrons or holes, which is described by the so-called Fröhlich interaction. In the Fröhlich model, the electron-transverse optical (TO) phonon coupling is neglected and the electron-longitudinal optical (LO) phonon coupling matrix element is given by[42]

$$g_{\mathbf{q}} = \frac{\mathrm{i}}{|\mathbf{q}|}\sqrt{\frac{e^2\hbar\omega_{LO}}{2\varepsilon_0\Omega}\left(\frac{1}{\kappa_\infty}-\frac{1}{\kappa_0}\right)}, \tag{8}$$

where $\mathbf{q}$ is the phonon wavevector, ε_0 is the vacuum permittivity, Ω is the volume of the unit cell, and κ_0 and κ_∞ are the static and high-frequency dielectric constants, respectively. When a dispersionless phonon is assumed, that is, the phonon frequency ω_{LO} is independent of $\mathbf{q}$, the scattering rate takes the form[35]

$$\begin{aligned}\frac{1}{\tau_{\mathbf{k}}} = \frac{e^2\omega_{LO}\left(\frac{1}{\kappa_\infty}-\frac{1}{\kappa_0}\right)}{4\pi\varepsilon_0\hbar\sqrt{2E_{\mathbf{k}}/m^*}}\Bigg[&N_\omega\sqrt{1+\frac{\hbar\omega_{LO}}{E_{\mathbf{k}}}}+(N_\omega+1)\sqrt{1-\frac{\hbar\omega_{LO}}{E_{\mathbf{k}}}}\\ &-\frac{\hbar\omega_{LO}N_\omega}{E_{\mathbf{k}}}\sinh^{-1}\left(\frac{\hbar\omega_{LO}}{E_{\mathbf{k}}}\right)^{1/2}\\ &+\frac{\hbar\omega_{LO}(N_\omega+1)}{E_{\mathbf{k}}}\sinh^{-1}\left(\frac{\hbar\omega_{LO}}{E_{\mathbf{k}}}-1\right)^{1/2}\Bigg],\end{aligned} \tag{9}$$

where N_ω is the occupation number of phonons with frequency ω. For details about the derivation of this equation, we refer the readers to Ref. 35. The Fröhlich model assumes an isotropic dielectric medium and only one polar LO mode that couples to the carriers. However, such conditions are clearly not satisfied in the case of SnO, SnO_2, and Ta_2SnO_6 where more than one LO modes exist. To incorporate crystal anisotropy and multiple LO modes scattering, we use the Vogl model,[43] which provides a more accurate description of electron-phonon coupling. The Vogl model has been widely used for describing the electron-optical phonon coupling in polar crystals.[34,43–45] Similar to the Fröhlich model, the key ingredient in the Vogl model is that it relates the perturbing potential induced by the optical phonons to the dielectric constants and the Born effective charges, both of which can be computed using DFT. In the Vogl model, the coupling matrix element is given by[34,44]

$$g_{\mathbf{q}}^\lambda = \mathrm{i}\frac{4\pi}{\Omega}\frac{e^2}{4\pi\varepsilon_0}\sum_j\sqrt{\frac{\hbar}{2M_j\omega_{\mathbf{q}}^\lambda}}\frac{\mathbf{q}\cdot\mathbf{Z}_j^*\cdot\mathbf{e}_{j\mathbf{q}}^\lambda}{\mathbf{q}\cdot\kappa_\infty\cdot\mathbf{q}}, \tag{10}$$

where M_j is the atomic mass of jth atom, $\mathbf{Z}_j^*$ is the born effective charge tensor, κ_∞ is the high-frequency dielectric constant tensor,

and $\mathbf{e}_{j\mathbf{q}}^{\lambda}$ is the eigendisplacement of atom j in phonon mode λ and is normalized according to $\sum_j \mathbf{e}_{j\mathbf{q}}^{\lambda'} \cdot \mathbf{e}_{j\mathbf{q}}^{\lambda} = \delta_{\lambda'\lambda}$. Note that the expression for the coupling matrix element shown here differs from that by Verdi and Giustino,[45] and in the latter, there is an extra integration term that can be simplified and reduced to ours when only the polar couplings are taken into account. The simplified expression is adopted since it can enable the scattering rates to be expressed analytically. The Vogl model here includes the directional dependence of the electron-phonon coupling in the sense that the coupling strength is proportional to the projection of the net dipole strength $\mathbf{Z}_j^* \cdot \mathbf{e}_{j\mathbf{q}}^{\lambda}$ along the direction of $\mathbf{q}$. The Vogl model also implies that the transverse optical (TO) phonon modes do not couple to the carriers since the $\mathbf{q} \cdot \mathbf{Z}_j^* \cdot \mathbf{e}_{j\mathbf{q}}^{\lambda}$ term becomes zero in those cases. In general, the anisotropy of coupling strength is determined by the combined symmetry of both phonon and electronic states. Incorporating such anisotropy for the calculation of scattering rate requires a numerical integration indicated by Eq. (3), and often a Wannier–Fourier (WF)[46] interpolation is needed to obtain a very fine resolution of the matrix elements for achieving convergence. Such scheme, however, is beyond the scope of this study. In this work, we will instead consider an "isotropic approximation" by approximating the anisotropic electron-phonon coupling matrix elements with appropriate $\mathbf{q}$-space angle-averaged quantities. This is implemented by the expression

$$\langle |g_{|\mathbf{q}|}^{\lambda}|^2 \rangle_{\theta,\varphi} = \frac{1}{4\pi} \int_{-1}^{1} d(\cos\theta) \int_{0}^{2\pi} d\varphi |g_{\mathbf{q}}^{\lambda}|^2, \tag{11}$$

where the brackets $\langle \cdot \rangle_{\theta,\varphi}$ denote averaging over the azimuthal angle θ and polar angle φ, performed numerically.

In addition, the Born effective charge is related with the static and high-frequency dielectric constants through[47]

$$\frac{1}{\kappa_0} = \frac{1}{\kappa_\infty} - \lim_{\mathbf{q}\to 0} \frac{1}{\kappa_\infty^2} \frac{4\pi}{\Omega} \frac{e^2}{4\pi\varepsilon_0} \sum_{\lambda} \left(\sum_j \frac{\mathbf{Z}_j^* \cdot \mathbf{e}_{j\mathbf{q}}^{\lambda}}{\sqrt{M_j}\omega_{\mathbf{q}}^{\lambda}} \right)^2, \tag{12}$$

where we have used the notations $(\kappa_0)^{-1} = 1/\kappa_0$ and $(\kappa_\infty)^{-1} = 1/\kappa_\infty$. As mentioned previously, due to the anisotropy of lattice vibration in SnO, SnO_2, and Ta_2SnO_6, the static dielectric constants are direction dependent. To simplify this, here, we adopted an isotropic approximation and a spatially averaged dielectric constant would be used, i.e., $\kappa_0 = (\kappa_{0,xx} + \kappa_{0,yy} + \kappa_{0,zz})/3$, where $\kappa_{0,xx}$, $\kappa_{0,yy}$, and $\kappa_{0,zz}$ are static dielectric constant along three Cartesian axes, respectively. The high-frequency dielectric constants, on the other hand, are usually nearly isotropic since the dielectric constants at high frequency are mainly contributed by electrons, as lattice ions cannot respond at high frequency.[48] Inserting Eq. (12) back into Eq. (10), we arrive at

$$g_{\mathbf{q}}^{\lambda} = \frac{\mathrm{i}}{|\mathbf{q}|} \sqrt{\frac{e^2\hbar\omega_{\mathbf{q}}^{\lambda}}{2\varepsilon_0\Omega} \left(\frac{1}{\kappa_\infty} - \frac{1}{\kappa_0} \right) \cdot w_{\mathbf{q}}^{\lambda}}, \tag{13}$$

where $w_{\mathbf{q}}^{\lambda}$ is given by

$$w_{\mathbf{q}}^{\lambda} = \frac{\left(\sum_j \frac{\mathbf{q} \cdot \mathbf{Z}_j^* \cdot \mathbf{e}_{j\mathbf{q}}^{\lambda}}{|\mathbf{q}|\sqrt{M_j}\omega_{\mathbf{q}}^{\lambda}} \right)^2}{\sum_{\lambda'} \left(\sum_j \frac{\mathbf{Z}_j^* \cdot \mathbf{e}_{j\mathbf{q}}^{\lambda'}}{\sqrt{M_j}\omega_{\mathbf{q}}^{\lambda'}} \right)^2}. \tag{14}$$

We note that in low-symmetry crystals, the longitudinal mode or transverse mode is not exactly parallel or perpendicular to the direction of $\mathbf{q}$. If we consider the strict LO (TO) modes in which the dipole strength $\mathbf{Z}_j^* \cdot \mathbf{e}_{j\mathbf{q}}^{\lambda}$ is parallel (perpendicular) to the wavevector $\mathbf{q}$, Eq. (14) will further reduce to

$$w_{\mathbf{q}}^{\lambda} = \frac{\left(\sum_j \frac{\mathbf{Z}_j^* \cdot \mathbf{e}_{j\mathbf{q}}^{\lambda}}{\sqrt{M_j}\omega_{\mathbf{q}}^{\lambda}} \right)^2}{\sum_{\lambda'} \left(\sum_j \frac{\mathbf{Z}_j^* \cdot \mathbf{e}_{j\mathbf{q}}^{\lambda'}}{\sqrt{M_j}\omega_{\mathbf{q}}^{\lambda'}} \right)^2}. \tag{15}$$

Compared with Eq. (8), Eq. (13) shows that in the case of multiple POP modes coupling, each mode contributes to the total coupling strength by the weight $w_{\mathbf{q}}^{\lambda}$. We note that if there is only one LO mode, Eq. (13) reduces correctly to the Fröhlich model in Eq. (8). Assuming the phonons are dispersionless, one obtains the relaxation time for multiple phonon modes scattering as

$$\frac{1}{\tau_{\mathbf{k}}} = \sum_{\lambda} \frac{w^{\lambda}}{\tau_{\mathbf{k}}^{\lambda}}, \tag{16}$$

with w^{λ} and $\tau_{\mathbf{k}}^{\lambda}$ given by Eqs. (14) and (9), respectively.

The scattering rates can be expressed analytically when the simplifications including parabolic energy bands, dispersionless optical phonons, and isotropic phonon scattering are introduced. Without these simplifications, scattering rates can only be evaluated by carrying out a series of numerical integrals of millions of electron-phonon coupling elements, which would be computationally very expensive. Parabolic band approximation is a very common practice in semiconductor physics, and it is also the essence of the effective mass approximation theory. For nondegenerate semiconductors under low-field transport, carriers are occupying the conduction/valence band edges that rationalize the parabolic band approximation. The dispersionless approximation is also called the Einstein model, where phonon frequency is regarded independent on the phonon wave vector $\mathbf{q}$. The simplified dispersion relation for optical modes is often used for scattering calculations. However, the "dispersionless approximation" in our model does not require that phonon mode be dispersionless or almost dispersionless. This is because the phonons involved in the scattering process are those with wave vector $\mathbf{q}$ near the center of the Brillouin zone due to momentum and energy conservation.[35] Since the energies associated with the phonons are significantly lower than those with the electrons, the final states that electrons are scattered into cannot differ too much from the initial states in terms of energies. This determines that within intraband scatterings, electron momentum differences cannot be large, which

implies that the scattering phonons are near the center of the Brillouin zone. In this regard, we can assume their frequencies are invariant when the wave vectors of phonons of interest only occupy a small range near the center of the Brillouin zone in the **q**-space. As for the isotropic approximation, we need to consider the directionality of both electron momentum state **k** and phonon wave-vector **q**, as the scattering rates depends on both quantities. The anisotropy of scattering rates due to the directionality of **k** turns out to be characterized by the anisotropy of the effective mass, and such anisotropy has already been taken into account in our evaluation model, as shown in Eq. (9). The anisotropy of electron-phonon coupling matrix elements arising from their **q** dependence is alleviated by using an average value to approximate those matrix elements of the spherical surface in the **q**-space. The matrix elements are dumped into an averaged value and will lead to an analytical integration, which avoids intensive computations needed for numerical integrations.

Nevertheless, such a simplified model and the assumptions inherent in it are subject to be substantiated. To further verify these approximations and evaluate how accurate the model is, we have tested our model in a wide range of compound semiconductors, including III-V semiconductors, II-VI semiconductors, and metal oxides. Table III lists the computed and experimental mobilities of these compound semiconductors, with related parameters needed for the calculation of mobilities also included. Note that all the material parameters, including effective masses, dielectric constants, and LO phonon frequencies, are experimental values, unless they are not available from literature studies, and in that case, the DFT predicted values are used instead. All of the experimental values are measured based on the single-crystal samples. Broadly speaking, the model gives quantitatively reasonable predictions for the mobilities in these tested compounds, though with a systematic overestimation when compared to the experiments (in general 1.5–2 times of the experimental values). The overestimations may come from the approximations assumed in the model and the ionized impurity scattering in the real samples, and it is hard to determine which factor is more dominant since the carrier concentrations in the experimental samples vary with a wide range. Nonetheless, our simulated mobilities are in fair agreement with experimental values from the engineers' point of view. With a simplified analytical expression and less intensive computations, our model would be rather helpful in the rapid prediction of the upper limit of the intrinsic mobilities of materials.

It is expected that different POP modes contribute differently to the total scattering rate. By plotting the mode-resolved coupling strength $g_{\mathbf{q}}^{\lambda}$ in Eq. (13) for different λ modes, one can visualize the detailed contributions of each mode to the total carrier scattering. Figure 1 shows the computed angularly averaged coupling matrix elements for different phonon modes at a fixed magnitude of $|\mathbf{q}| = 0.05\,2\pi/a$ (a is a lattice constant) for SnO, SnO_2, and Ta_2SnO_6. Because the calculated phonon eigenvectors are not exactly parallel or perpendicular to **q**, we calculate coupling matrix elements for all the optical phonon modes that appear in the phonon dispersion. We can see that in these three crystals, different modes make different contributions, with some modes accounting for almost total coupling strength, while other modes contributing only marginally. Specifically, in SnO, the phonon mode $w^{\lambda} = 30.3$ meV accounts for nearly 100% of the total coupling strength, with the remaining modes giving two orders of magnitude smaller coupling. Predictably, this vibration mode will play the dominant role in determining the POP mobility of SnO. In SnO_2, however, several significantly strong couplings are observed, for example, 27.3 meV, 32.5 meV, 68.6 meV, and 72.7 meV. When compared with SnO and SnO_2, Ta_2SnO_6 shows more dispersed coupling strengths among different modes, which might result from the asymmetry of its crystal structure. Another interesting finding is that although SnO and SnO_2 exhibit mode degeneracy due to tetragonal symmetry, these degenerate modes do not give the same coupling strength. A closer look at the phonon

TABLE III. POP-limited motility model test in GaAs, ZnO, PbS, In_2O_3, and TiO_2. The effective mass m^*, static dielectric constant κ_0, high-frequency dielectric constant κ_∞, and LO phonon frequency ω_{LO} are experiment values, unless they are not available from literature studies, and in that case, the DFT predicted values are used instead (denoted by *). In compounds with a hexagonal or tetragonal crystal structure, the effective mass and dielectric constant exhibit two distinct values along the *c*-axis (||) and in-plane (⊥) directions. The characteristics of the LO mode in the crystals, whether isotropic or anisotropic and whether single LO mode or multiple LO modes, are also indicated. For a fair comparison, the experimental measured mobilities are from single-crystal samples.

		$m^*(m_0)$		Dielectric constant				μ (cm^2/V s) calc.		μ (cm^2/V s) expt.	
System	Crystal structure	e	h	κ_0	κ_∞	ω_{LO} (cm^{-1})	LO mode	e	h	e	h
GaAs[49]	Zinc Blende (cubic)	0.067	0.51	12.9	10.89	291	Isotropic Single	12234	949	8500	400
ZnO[50]	Wurtzite (hexagonal)	0.29	0.78	7.77(⊥) 8.91(||)	3.68(⊥) 3.72(||)	583(⊥) 574 (||)	Anisotropic Multiple	365	82.7	205	50
PbS[51]	Halite (cubic)	0.18*	0.16*	169	15.2	202	Isotropic single	760	861	600[52]	600[52]
In_2O_3[53]	Bixbyite (cubic)	0.30[6]	2.87*	8.9[54]	4.1[54]	245* 196* 194* 161*	Isotropic multiple	342	11.6	160	…
TiO_2[55]	Anatase (tetragonal)	0.45*(⊥) 4.54*(||)	2.19*(⊥) 1.03*(||)	45.1(⊥) 22.7(||)	5.4(⊥) 5.8(||)	876(⊥) 366(⊥) 755(||)	Anisotropic Multiple	81.5(⊥) 2.55(||)	7.62(⊥) 24.2(||)	18[56]	…

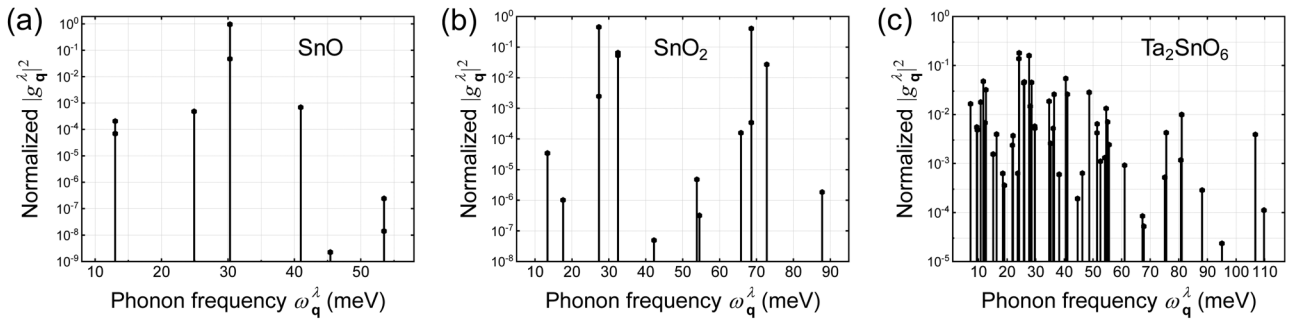

FIG. 1. The electron-phonon coupling matrix elements for each POP (both LO and TO) mode at $|\mathbf{q}| = 0.05\,2\pi/a$ (a is the lattice constant) in SnO, SnO_2, and Ta_2SnO_6. The squared modulus of coupling matrix elements is used and normalized according to $1 = \sum_{\lambda} (g_{\mathbf{q}}^{\lambda})^2$.

structures of SnO and SnO_2 reveals that those frequency-degenerate modes do not assume degenerate or equivalent eigendisplacements, which would account for the different coupling strength. In Ta_2SnO_6, however, because of the monoclinic crystal nature, no degenerate modes are observed.

Next, we calculated the scattering rates at room temperature for different POP modes in SnO, SnO_2, and Ta_2SnO_6. As discussed previously, the matrix elements show the direction dependence, and we thus adopted a spherically averaging approximation. The resulting scattering rates with $\mathbf{k}$ along the z-direction are shown in Fig. 2. For each material, the total scattering rate as well as scattering rates by several strong coupling branches are plotted. The contribution to the total scattering rate by each mode in SnO, SnO_2, and Ta_2SnO_6 is consistent with the result shown in Fig. 1. In SnO, the total scattering rate for holes moving along the z-direction almost follows that of the phonon mode $w^{\lambda} = 30.3$ meV because this mode is responsible for nearly all the scattering events. Since the POP scattering includes both phonon absorption and emission processes, the scattering rate for each mode clearly shows the kink at the point of phonon energy, which corresponds to the onset of phonon emission. By comparing the two modes 27.3 and 68.6 meV that give the similar coupling strength in SnO_2, we found that the 27.3 meV low-energy phonon mode is more effective in scattering. This is because low-energy phonon modes are efficiently activated at room temperature and provide two scattering channels (absorption and emission) for electrons near the Fermi level. The scattering rate gradually drops at higher electron/hole energy, due to the decreased available density of states that carriers can be scattered into. Figure 2 also shows the carrier distribution obtained by combining the Fermi-Dirac distribution function and electron/hole DOS. The energy range that shows a high electron/hole distribution will be more relevant to the averaged relaxation time, as indicated by Eq. (2).

The POP mobilities at room temperature for SnO, SnO_2, and Ta_2SnO_6 were then calculated, as listed in Table IV. Generally, in polar crystals, the POP is the dominant scattering mechanism limiting the room-temperature intrinsic mobilities.[35] In our results, the POP mobilities are much lower than the ADP mobilities agreeing with the expectation. To compare with experimental data, we also calculated the POP-limited Hall mobility. The Hall mobility differs from the drift mobility by the so-called Hall factor, which can be calculated as $r_H = \langle\langle \tau^2 \rangle\rangle / \langle\langle \tau \rangle\rangle^2$, where double brackets represent energy-weighted average as indicated in Eq. (2). Since POP scattering is the limiting factor, we will use our calculated POP mobilities

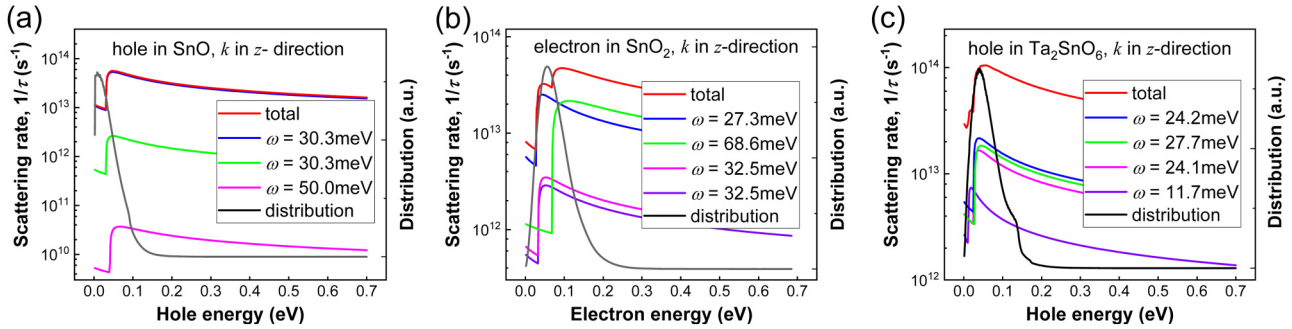

FIG. 2. Total scattering rates and the contributions by several strong coupling branches in SnO, SnO_2, and Ta_2SnO_6. The carrier distributions are also plotted to the right y-axis. Only electrons/holes moving along the z-direction are presented.

TABLE IV. The static and high-frequency dielectric constants κ_0 and κ_∞, POP-limited mobilities μ_{POP}, mobilities limited by both ADP and POP in SnO, SnO_2, and Ta_2SnO_6, Hall factors r_H, averaged Hall mobilities μ_{Hall} (ave) limited by POP, and the experimentally determined Hall mobilities μ_H (expt.).

		κ_0			κ_∞			μ_{POP} (cm^2/V s)			$\mu_{POP+ADP}$ (cm^2/V s)					
System		x	y	z	x	y	z	x	y	z	x	y	z	r_H	μ_{Hall} (ave)	μ_{Hall} (expt.)
SnO	e	21.7	21.7	11.8	7.0	6.4	6.4	289	289	128	280	280	125	1.30	306	…
	h							9.4	9.4	94.4	7.4	7.4	60.0	1.77	66.8	1–18[6,16,31,61]
SnO_2	e	13.0	13.0	8.8	4.0	4.0	4.3	170	170	235	166	166	229	1.38	265	240[57]
	h							15.8	15.8	11.1	15.7	15.7	11.0	1.37	19.5	…
Ta_2SnO_6	e	38.8	35.7	60.0	5.7	5.6	5.8	6.4	0.2	27.8	6.3	0.2	27.1	1.14	13.0	…
	h							0.9	33.8	21.3	0.9	32.5	20.6	1.09	20.4	…

to compare with experiments. For SnO, we obtain the hole mobilities of 9.4 and 94.4 cm^2/(V s) for x- and z-directions, respectively, leading to an average hole mobility of 38 cm^2/(V s). Correspondingly, the p-type Hall mobility averages out at 67 cm^2/(V s). In comparison, experiments have so far achieved room-temperature hole drift mobilities ranging from 0.1 to 10 cm^2/(V s) and Hall mobilities from 1 to 18 cm^2/(V s), depending on the materials' crystallinity and the device geometries.[6,17,18] Our results are in fair agreement with the reported experimental value, if one considers that other extrinsic factors such as ionized impurity scattering are expected to exist in experimental samples. For electrons in SnO_2, our calculated drift mobility varies from 170 cm^2/(V s) in the x-direction to 235 cm^2/(V s) in the z-direction, with spatially averaged value at 192 cm^2/(V s). This results in an averaged Hall mobility of 265 cm^2/(V s), which agrees well with the experimental value at 300 K [240 cm^2/(V s)] as well as other theoretical calculations [310 cm^2/(V s)].[57] For Ta_2SnO_6, there has been an experimental report on the electrical characterization of the Sn-O-Ta compound, but only with the $Ta_2Sn_2O_7$ stoichiometry.[21] The measured mobility for $Ta_2Sn_2O_7$ [~0.1 cm^2/(V s)] stands much lower than our predicted mobility for $TaSn_2O_6$ due to the more flat valence band and the resulting larger effective hole mass in $Ta_2Sn_2O_7$.[58] Finally, we calculated the total mobility taking both ADP and POP into account, as presented in Table IV. For all these materials, the phonon-limited intrinsic mobilities are close to the POP mobilities, indicating that POP plays a dominant role in carrier scattering.

D. Discussion

Although a spherical averaging approximation was adopted in treating the anisotropy of lattice vibrations, the carrier mobilities in SnO, SnO_2, and Ta_2SnO_6 are still highly anisotropic, due to the strong anisotropy of the electronic structure, i.e., effective mass. This is manifested by the almost 10 times difference of hole mobility in different directions in SnO. The tetragonal layer-structured SnO shows only two hole effective masses: $0.64m_0$ along the z-direction (interlayer) and $2.98m_0$ in the plane perpendicular to the former direction (intralayer). The smaller effective mass in the interlayer direction leads to a higher mobility along the direction, in contrast to other 2D materials such as MoS_2 where intralayer transport is often superior than interlayer transport.[59] Compared with SnO and SnO_2, Ta_2SnO_6 shows relatively low room-temperature mobilities for both electron and hole due to the large effective masses, which in turn suggests that the effective masses account for the differences in the mobilities in different materials.

Interestingly, our results show that SnO exhibits an excellent electron mobility with an average value of 228 cm^2/(V s). This value is even higher than that in n-type SnO_2 where electron mobility averages out at 187 cm^2/(V s). This finding may motivate experimentalists to incorporate SnO as a n-type semiconductor into the already realized unipolar p-type SnO-based transistors to implement high-performance complementary circuits. Currently, oxide semiconductor research community is searching for promising p-type oxides with good mobility as they remain elusive. SnO_2 has been proposed as a potential p-type oxide due to its compatibility with the commercialized n-type SnO_2-based electronics. However, the acceptor doping for p-type SnO_2 has recently proven unachievable, due to the hole trap center formation associated with the acceptor defects.[60] Since SnO has been identified as a p-type oxide candidate, if validated having good n-type doping ability, it could be potentially introduced as a bipolar semiconductor into oxide electronics that requires both n-type and p-type MO materials. Further studies would be focused on the investigation of n-doping achievable in SnO.

SnO is expected to exhibit good hole mobility due to its relatively low effective hole mass resulted by the hybridization of pseudo-closed $5s^2$ orbitals of Sn^{2+} and oxygen $2p$ orbitals.[6] However, our calculated result shows that the highest possible hole mobility for SnO stands at 60 cm^2/(V s), slightly lower than the targeted value of 100 cm^2/(V s) to be considered a high-mobility p-type oxide. Ta_2SnO_6 shows even lower hole mobility than SnO, indicating a necessity of further investigation to discover higher mobility p-type oxides. Alternative compounds can be identified through searching for the materials with even lower hole effective masses. This can be implemented based on the screening rule that VBM are largely occupied by the delocalized s-orbital of nontransition metal (TM) or d-orbital of TM. A few novel materials including B_6O, $A_2Sn_2O_3$ (A = K, Na), and ZrOS have recently been identified as low-effective-mass oxides according to such rule.[14] However, their mobilities are subject to further investigation, as mobilities are also influenced by various scattering mechanisms.

IV. CONCLUSION

In conclusion, we employed a first-principles approach to calculate intrinsic phonon-limited mobilities for Sn-based oxide

semiconductors including *p*-type SnO and Ta_2SnO_6 and *n*-type SnO_2. Having considered multiphonon modes scattering, room-temperature electron/hole mobilities in these oxides are found to be predominantly limited by the POP scattering. Our results agree well with previous theoretical calculations and experimental data for SnO and SnO_2. Although *p*-type SnO exhibits an excellent electron mobility, the upper limit for its hole mobility stands only at 60 $cm^2/(V\,s)$, slightly lower than the threshold value of 100 $cm^2/(V\,s)$ to be considered a high-mobility *p*-type oxide for vertical CMOS. SnO_2 shows good electron mobility with an average value of 192 $cm^2/(V\,s)$, confirming its promise as an *n*-type semiconductor. *p*-type Ta_2SnO_6 shows lower hole mobility than SnO, indicating a necessity of further investigation to discover higher mobility *p*-type oxides. Calculated effective masses directly correlate with the differences in mobilities of different materials, which make it an effective screening criterion in searching for high-mobility *p*-type oxides.

ACKNOWLEDGMENTS

The authors would like to thank C. Zhang and Y. Nie for their helpful suggestions and discussions. This work was supported by ASCENT, one of the six centers in JUMP, a Semiconductor Research Corporation (SRC) program sponsored by Defense Advanced Research Projects Agency (DARPA). This work was also supported by National Research Foundation (NRF) of Korea by Creative Materials Discovery Program (No. 2015M3D1A1068062).

REFERENCES

[1]S. Salahuddin, K. Ni, and S. Datta, Nat. Electron. **1**, 442 (2018).
[2]M. M. Shulaker, G. Hills, R. S. Park, R. T. Howe, K. Saraswat, H.-S. P. Wong, and S. Mitra, Nature **547**, 74 (2017).
[3]T. F. Wu, H. Li, P.-C. Huang, A. Rahimi, G. Hills, B. Hodson, W. Hwang, J. M. Rabaey, H.-S. P. Wong, and M. M. Shulaker, IEEE J Solid State Circuits **53**, 3183 (2018).
[4]M. S. Ebrahimi, G. Hills, M. M. Sabry, M. M. Shulaker, H. Wei, T. F. Wu, S. Mitra, and H.-S. P. Wong, "Monolithic 3D integration advances and challenges: From technology to system levels," in *2014 SOI-3D-Subthreshold Microelectronics Technology Unified Conference (S3S)*, Millbrae, CA, *6–9 October 2014* (IEEE, 2014), p. 1.
[5]M. M. Shulaker, T. F. Wu, A. Pal, L. Zhao, Y. Nishi, K. Saraswat, H.-S. Philip Wong, and S. Mitra, "Monolithic 3D integration of logic and memory: Carbon nanotube FETs, resistive RAM, and silicon FETs," in *2014 IEEE International Electron Devices Meeting*, San Francisco, CA, *15–17 December 2014* (IEEE, 2014), p. 27.4.1.
[6]Y. Ogo, H. Hiramatsu, K. Nomura, H. Yanagi, T. Kamiya, M. Hirano, and H. Hosono, Appl. Phys. Lett. **93**, 032113 (2008).
[7]E. Fortunato, R. Barros, P. Barquinha, V. Figueiredo, S.-H. K. Park, C.-S. Hwang, and R. Martins, Appl. Phys. Lett. **97**, 052105 (2010).
[8]K. Nomura, H. Ohta, A. Takagi, T. Kamiya, M. Hirano, and H. Hosono, Nature **432**, 488 (2004).
[9]E. Fortunato, P. Barquinha, and R. Martins, Adv. Mater. **24**, 2945 (2012).
[10]K. Ellmer, Nat. Photonics **6**, 809 (2012).
[11]L. Petti, N. Münzenrieder, C. Vogt, H. Faber, L. Büthe, G. Cantarella, F. Bottacchi, T. D. Anthopoulos, and G. Tröster, Appl. Phys. Rev **3**, 021303 (2016).
[12]J. K. Jeong, J. H. Jeong, H. W. Yang, J.-S. Park, Y.-G. Mo, and H. D. Kim, Appl. Phys. Lett. **91**, 113505 (2007).
[13]C. G. Granqvist, Sol. Energy Mater. Sol. Cells **91**, 1529 (2007).
[14]G. Hautier, A. Miglio, G. Ceder, G.-M. Rignanese, and X. Gonze, Nat. Commun. **4**, 2292 (2013).
[15]S. Sheng, G. Fang, C. Li, S. Xu, and X. Zhao, Phys. Status Solidi A **203**, 1891 (2006).
[16]A. Banerjee and K. Chattopadhyay, Prog. Cryst. Growth Charact. Mater **50**, 52 (2005).
[17]W. Guo, L. Fu, Y. Zhang, K. Zhang, L. Liang, Z. Liu, H. Cao, and X. Pan, Appl. Phys. Lett. **96**, 042113 (2010).
[18]J. Caraveo-Frescas and H. N. Alshareef, Appl. Phys. Lett. **103**, 222103 (2013).
[19]M. V. Frischbier, H. F. Wardenga, M. Weidner, O. Bierwagen, J. Jia, Y. Shigesato, and A. Klein, Thin Solid Films **614**, 62 (2016).
[20]S. Nakao, N. Yamada, T. Hitosugi, Y. Hirose, T. Shimada, and T. Hasegawa, Appl. Phys. Express **3**, 031102 (2010).
[21]N. Kikuchi, A. Samizo, S. Ikeda, Y. Aiura, K. Mibu, and K. Nishio, Phys. Rev. Mater. **1**, 021601 (2017).
[22]See https://materialsproject.org/materials/mp-3593/ for more information about the band structure and formation energy about $Sn_2Ta_2O_7$.
[23]K. Kaasbjerg, K. S. Thygesen, and K. W. Jacobsen, Phys. Rev. B **85**, 115317 (2012).
[24]G. Kresse and J. Hafner, Phys. Rev. B **47**, 558 (1993).
[25]G. Kresse and J. Furthmüller, Phys. Rev. B **54**, 11169 (1996).
[26]G. Kresse and J. Hafner, J. Phys. Condens. Matter **6**, 8245 (1994).
[27]G. Kresse and D. Joubert, Phys. Rev. B **59**, 1758 (1999).
[28]A. Togo and I. Tanaka, Scr. Mater **108**, 1 (2015).
[29]J. Paier, M. Marsman, K. Hummer, G. Kresse, I. C. Gerber, and J. G. Ángyán, J. Chem. Phys. **124**, 154709 (2006).
[30]K. Govaerts, R. Saniz, B. Partoens, and D. Lamoen, Phys. Rev. B **87**, 235210 (2013).
[31]J. Pannetier and G. Denes, Acta Cryst. B **36**, 2763 (1980).
[32]H. Peng, J. D. Perkins, and S. Lany, Chem. Mater. **26**, 4876 (2014).
[33]K. Sundaram and G. Bhagavat, J. Phys. D Appl. Phys. **14**, 921 (1981).
[34]J. Sjakste, N. Vast, M. Calandra, and F. Mauri, Phys. Rev. B **92**, 054307 (2015).
[35]M. Lundstrom, *Fundamentals of Carrier Transport* (Cambridge University Press, 2009).
[36]J. Bardeen and W. Shockley, Phys. Rev. **80**, 72 (1950).
[37]W. Perger, J. Criswell, B. Civalleri, and R. Dovesi, Comput. Phys. Commun. **180**, 1753 (2009).
[38]J. Xi, M. Long, L. Tang, D. Wang, and Z. Shuai, Nanoscale **4**, 4348 (2012).
[39]V.-A. Ha, F. Ricci, G.-M. Rignanese, and G. Hautier, J. Mater. Chem. C **5**, 5772 (2017).
[40]C.-M. Liu, X.-R. Chen, and G.-F. Ji, Comput. Mater. Sci. **50**, 1571 (2011).
[41]Y. Mi, H. Odaka, and S. Iwata, Jpn. J. Appl. Phys. **38**, 3453 (1999).
[42]H. Fröhlich, Adv. Phys. **3**, 325 (1954).
[43]P. Vogl, Phys. Rev. B **13**, 694 (1976).
[44]Y. Kang, K. Krishnaswamy, H. Peelaers, and C. G. Van de Walle, J. Phys. Condens. Matter **29**, 234001 (2017).
[45]C. Verdi and F. Giustino, Phys. Rev. Lett. **115**, 176401 (2015).
[46]J. Noffsinger, F. Giustino, B. D. Malone, C.-H. Park, S. G. Louie, and M. L. Cohen, Comput. Phys. Commun. **181**, 2140 (2010).
[47]J. Kurkijärvi and D. Rainer, *The Dielectric Function of Condensed Systems* (Elsevier, 1989), Vol. 24, p. 293.
[48]Y. Kang, K. Krishnaswamy, H. Peelaers, and C. G. Van de Walle, J. Phys. Condens. Matter. **29**, 234001 (2017).
[49]See http://www.ioffe.ru/SVA/NSM/Semicond/GaAs/ for more information about the effective mass, dielectric constant, optical phonon frequency and mobility about GaAs.
[50]V. Coleman and C. Jagadish, in *Zinc Oxide Bulk, Thin Films and Nanostructures* , edited by C. Jagadish and S. Pearton (Elsevier, 2006), p. 1.
[51]O. Madelung, U. Rossler, and M. Schulz, *Non-Tetrahedrally Bonded Elements and Binary Compounds* (Springer, 1998), Vol. 41.

[52]See http://www.matweb.com/search/datasheet_print.aspx?matguid=d2f30ef191544dab92b5167e1afd1195 for more information about the mobility of PbS.
[53]R. Weiher, J. Appl. Phys. **33**, 2834 (1962).
[54]A. Schleife, M. D. Neumann, N. Esser, Z. Galazka, A. Gottwald, J. Nixdorf, R. Goldhahn, and M. Feneberg, New J. Phys. **20**, 053016 (2018).
[55]R. Gonzalez, R. Zallen, and H. Berger, Phys. Rev. B **55**, 7014 (1997).
[56]T. S. Krasienapibal, T. Fukumura, Y. Hirose, and T. Hasegawa, Jpn. J. Appl. Phys. **53**, 090305 (2014).
[57]C. Fonstad and R. Rediker, J. Appl. Phys. **42**, 2911 (1971).
[58]Y. Hosogi, Y. Shimodaira, H. Kato, H. Kobayashi, and A. Kudo, Chem. Mater. **20**, 1299 (2008).
[59]V. K. Sangwan and M. C. Hersam, Annu. Rev. Phys. Chem. **69**, 299 (2018).
[60]D. O. Scanlon and G. W. Watson, J. Mater. Chem. **22**, 25236 (2012).
[61]A. B. Mei, L. Miao, M. J. Wahila, *et al.* Phys. Rev. Mater. **3**, 105202 (2019).